

Tunable chiral spin texture in magnetic domain-walls

J. H. Franken, M. Herps, H. J. M. Swagten,* and B. Koopmans

*Department of Applied Physics, Center for NanoMaterials,
Eindhoven University of Technology, P.O. Box 513, 5600 MB Eindhoven, The Netherlands*

Magnetic domain-walls (DWs) with a preferred chirality exhibit very efficient current-driven motion [2, 3]. Since structural inversion asymmetry (SIA) is required for their stability, the observation [4] of chiral domain walls in highly symmetric Pt/Co/Pt is intriguing. Here, we tune the layer asymmetry in this system and observe, by current-assisted DW depinning experiments, a small chiral field which sensitively changes. Moreover, we convincingly link the observed efficiency of DW motion to the DW texture, using DW resistance as a direct probe for the internal orientation of the DW under the influence of in-plane fields. The very delicate effect of capping layer thickness on the chiral field allows for its accurate control, which is important in designing novel materials for optimal spin-orbit-torque-driven DW motion.

Current-induced motion of magnetic DWs in materials with perpendicular magnetic anisotropy (PMA) could be used to transport data in next-generation storage devices [5]. Recently, it has been suggested that in addition to conventional bulk STT contributions [6], various current-induced torques relating to the high spin-orbit coupling in these materials could play a dominant role [7–9]. Most notably, the sources of these so-called spin orbit torques include the Rashba field, which enters as a current-dependent transverse H_y field [10–12], and the spin Hall effect [13], which leads to a vertical spin current with transverse polarization σ_y . In a previous work [1], we demonstrated that the Spin Hall effect has the correct characteristics to describe the effect of current on domain walls in Pt/Co/Pt. It was observed that the efficiency of current-induced DW motion is practically zero, since the Bloch wall that is expected to be stable does not have the correct symmetry to be moved by a SHE-induced torque (Figure 1(a)), i.e. the cross product of the injected spin direction and magnetization direction within the DW vanishes [1, 15]. Efficient motion arose when the internal structure was forced to the Néel type by applying a field along the current direction. However, this still contradicts the uniform motion of all DWs, at zero in-plane field, that was observed in other materials where the magnetic layer was sandwiched between two different materials [10, 16, 17]. Subsequently, it was recognized by several authors [2, 3, 18, 19] that in the case of structural inversion asymmetry (SIA), the

Dzyaloshinskii-Moriya interaction (DMI) [20] gives rise to chiral spin structures, in this case chiral Néel walls [21–23], which are moved uniformly by a spin-Hall-effect-induced effective field (H_{SHE} in Figure 1(b)).

In this work, we demonstrate by current-assisted depinning measurements that a measurable DMI is also present in Pt/Co/Pt [4], which is surprising at first since the top and bottom interfaces are in principle the same. The DMI effect is found to be highly tunable by varying the top layer thickness, and becomes very large when the top Pt layer is substituted by AlOx. In fact, the tuning is so delicate that the DW can have any in-plane angle ϕ in between the Bloch ($\phi = \frac{\pi}{2}$) and Néel ($\phi = 0$) states at remanence, due to the competition between the effective longitudinal DMI field H_D and transverse DW anisotropy field H_K , as visualized in Figure 1(c). Our data can be explained by a very simple model [3] of the internal DW angle ϕ under influence of H_D , H_K , and externally applied in-plane fields H_x and H_y (Figure 1(d)). The efficiency of DW depinning is simply proportional to $\cos \phi$, as expected from a field-like torque by the SHE [3]. To prove that the DW angle ϕ is responsible for the efficiency, we measure the DW resistance as a function of in-plane fields (Figure 1(e)) and observe that the DW structure is indeed changing from Bloch to Néel, which is often just assumed based on elementary micromagnetics without any convincing experimental proof. These measurements allow us to directly correlate a high DW efficiency to the presence of Néel walls, which we show to be stabilized by the DMI in a tunable way.

To allow for DW resistance as well as DW depinning measurements, $1.5 \mu\text{m}$ wide strips with varying layer configurations were fabricated. Irradiation with Ga ions is employed to locally reduce the PMA in $1.5 \mu\text{m}$ long areas in these strips, allowing us to introduce a well-defined number of DWs into the strip [7, 24]. The Kerr microscopy image in Figure 1(e) visualizes the controlled domain structure that is essential for the DW resistance measurements presented later. When the perpendicular field strength is increased from this state, DWs are randomly depinning from the edges of the irradiated regions, as indicated in Figure 1(f). We analyze the effect of current on the depinning of two particular DWs, indicated by the red circle and blue square in Figure 1(f). The graph shows how the depinning field of these domain walls change with increasing current density in a Pt(4)/Co(0.4)/Pt(2) sample (all thicknesses in nm). The slopes define the depinning efficiency $\epsilon = \mu_0 \frac{dH_{\text{SHE}}}{dJ}$ of each DW. The opposing slopes of the 2 DWs actually imply a small but uniform action of the current on the DWs: since the field pushes both DWs outwards (in op-

* h.j.m.swagten@tue.nl

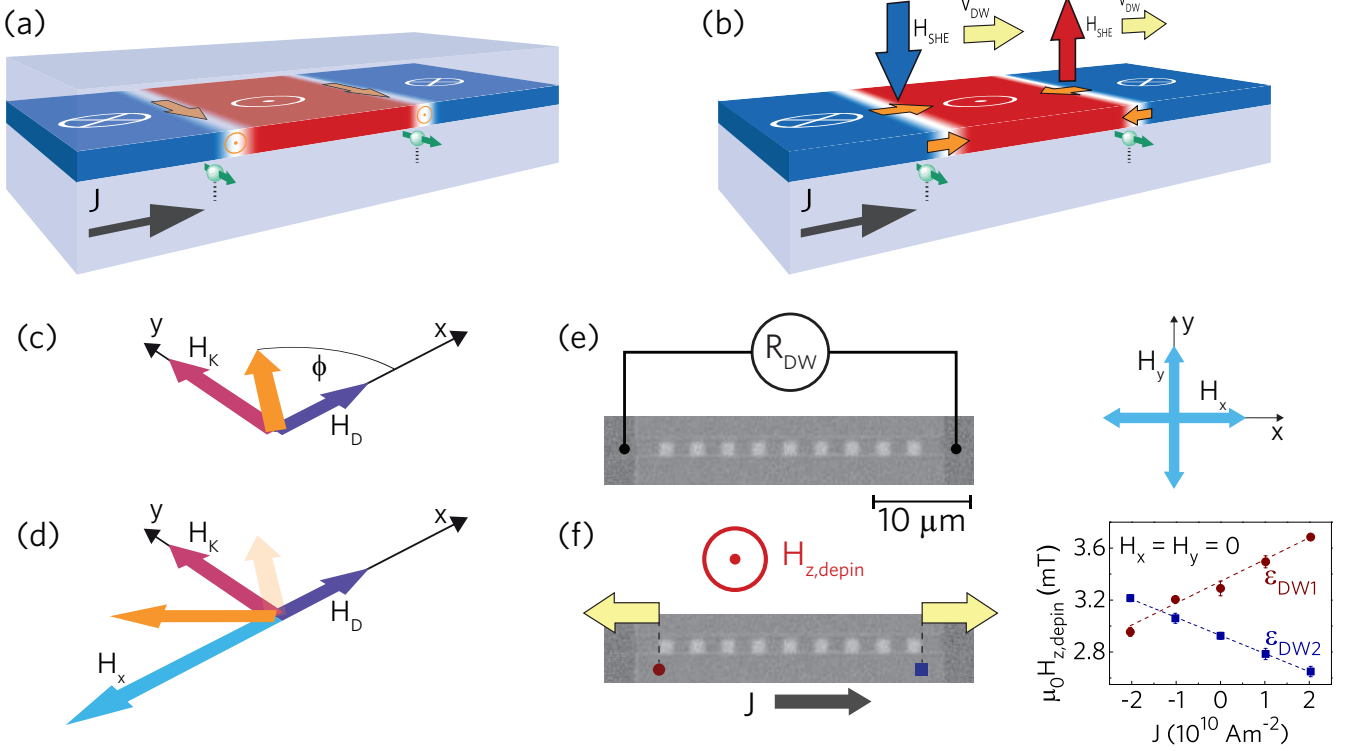


FIG. 1. Tuning the chirality of magnetic DWs. (a) In a symmetric layer system, Bloch walls are favored (orange arrows), on which the spin Hall current (green spins) cannot exert a torque. (b) If SIA is introduced, chiral Néel walls with alternating orientation become stable, which are moved uniformly (yellow arrows) by the effective spin Hall field $H_{SHE} \propto \cos \phi$. (c) The in-plane DW angle ϕ (orange) is determined by the competition of the DMI field H_D (violet) and the DW anisotropy field H_K (pink). (d) The internal angle can be further tuned using an external magnetic field H_x (light blue) or H_y (not shown). (e) DW resistance measurements can be used to verify the DW angle ϕ under influence of H_x and H_y . This can be linked to DW motion measurements on the same samples (f), where the depinning field $H_{z,depin}$ as a function of current density J is measured for the two outermost DWs. The slope of this relation defines the depinning efficiency ϵ of each DW, which scales with $\cos \phi$. The Kerr micrographs show the well-controlled alternating pattern of up (white) and down (grey) domains, realized by Ga irradiation of the white areas.

posite directions), the current reduces the depinning field of DW2 (negative efficiency) and increases the depinning field of DW1 (positive efficiency). It is worth noting that the sign of current-induced domain wall motion opposes the electron flow direction and is therefore unlikely to be caused by conventional STT. Instead, we propose that the DWs have a small degree of built-in chirality, which leads to their uniform motion driven by the SHE. This is a refinement to our observations on similar samples in [1], where we assumed that domain-walls are of the non-chiral Bloch type at zero in-plane field. To prove the presence of a favored chirality in Pt/Co/Pt, we will use in-plane fields to either oppose or assist the built-in chiral field H_D .

Figure 2 shows the measured current-induced depinning efficiency $\epsilon(H_x)$ (top panes) and $\epsilon(H_y)$ (bottom panes) on three samples with different compositions. We first discuss Figure 2(a-b), representing the sample with the lowest degree of inversion asymmetry, Pt(4)/Co(0.4)/Pt(2). The H_x and H_y data have been fitted simultaneously using the efficiency expected from

the 1D-model with only the SHE as driving force [3],

$$\epsilon = \mu_0 \frac{dH_{SHE}}{dJ} = \frac{\pi \hbar \nu \theta_{SH}}{4eM_s t} \cos \phi =: \epsilon_{SHE} \cos \phi, \quad (1)$$

with θ_{SH} the spin Hall angle, M_s the saturation magnetization, t the magnetic layer thickness, ν a loss factor due to compensating spin Hall currents from the bottom and top Pt layers [1], and ϕ the internal DW angle prescribed by energy minimization of

$$E_{DW} = \lambda \mu_0 M_s \left(H_K \cos^2 \phi - 2 \left(H_D + \frac{\pi}{2} H_x \right) \cos \phi - \pi H_y \sin \phi \right). \quad (2)$$

Here, λ is the DW width (assumed constant), H_K the shape anisotropy field of the DW, and $H_D = \pi D / (2\mu_0 M_s \lambda)$ the effective chiral magnetic field (with D an energy constant characterizing the strength of the DMI). The free parameters of the fit are H_K , H_D , and ϵ_{SHE} as indicated in Figure 2(a). This graph clearly shows that there is a contribution from DMI: the red

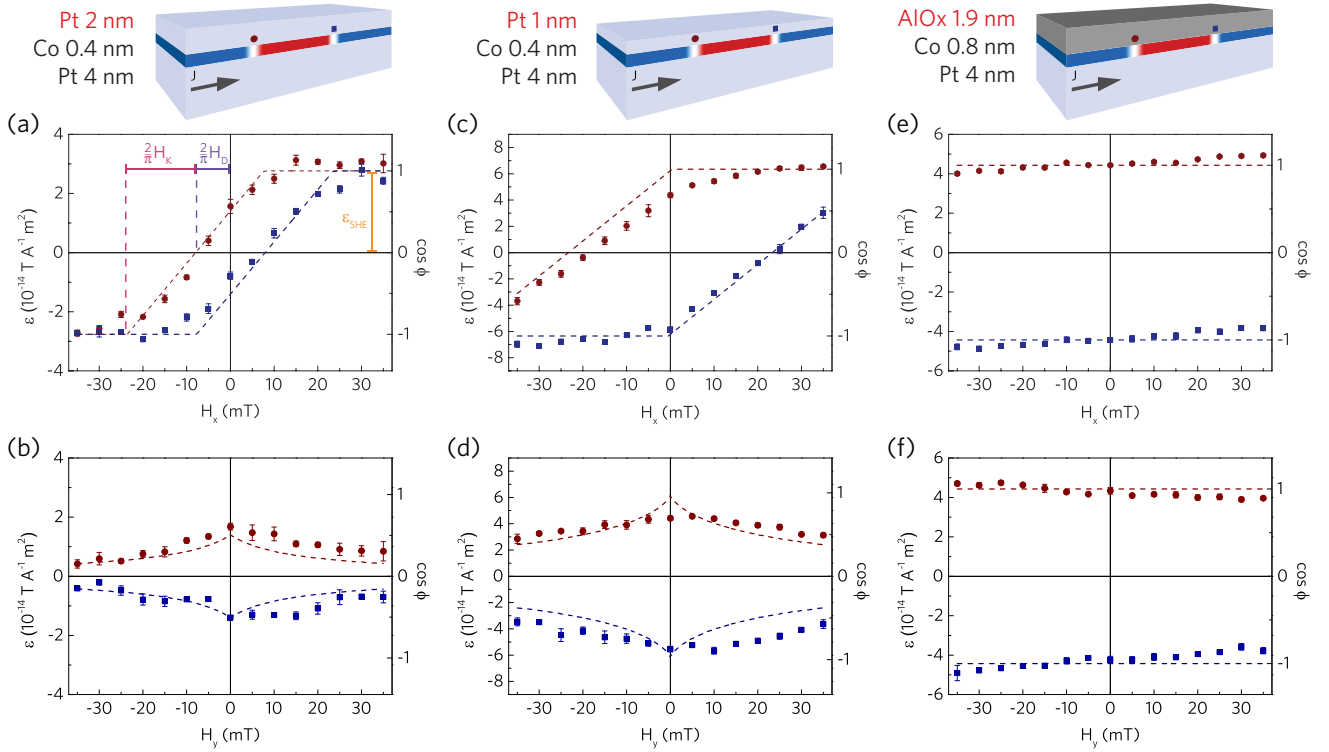


FIG. 2. Depinning efficiency ϵ under in-plane fields in systems with varying SIA. (a) in almost symmetric Pt(4)/Co(0.4)/Pt(2), $\epsilon(H_x)$ shows a small opening between the two domain walls (red discs and blue squares) of opposite polarity, indicative of a DMI field H_D . The slope of the transition from $\epsilon = 0$ to its saturation level ϵ_{SHE} is characterized by the DW anisotropy H_K . To determine these parameters, a global fit (dashed lines) is performed together with the H_y -data in (b). (c,d) Increasing the stack asymmetry by reducing the top Pt layer to 1 nm gives a higher DMI opening. (e,f) Replacing the top Pt layer by AIOx, the DMI opening becomes too large to measure in our setup. The DMI is so strong that the DW angle ϕ is hardly influenced by H_x and H_y . The fit corresponds to the average level.

and blue curves have been shifted to the left and right, respectively, due to the effective chiral magnetic field $H_D \approx 12.5 \pm 0.4$ mT, which has opposite sign for domain walls of opposite polarity (up-down vs down-up). We should note that H_D could be lower than in an unpatterned film, since the Ga irradiation locally reduces the anisotropy and increases λ . Apart from the observed horizontal shift, there is a linear increase from $\epsilon = 0$ to ϵ_{SHE} over a field range $\pi H_K/2$, which is attributed to the transition from Bloch to Néel. Replacing H_x by H_y in Figure 2(b), the efficiency simply decreases with $|H_y|$, because H_y gradually pulls the wall to a Bloch state. Interestingly, the DW at zero in-plane field is neither a Bloch nor a Néel wall. From the efficiency at zero in-plane field, it can be deduced that the DW angle at remanence is $\phi \approx 60^\circ$, rather than the 90° that is expected in a system without SIA. The stability of such an in-between wall type, observed before on epitaxial Co/Ni multilayers [23], might be interesting for specific device applications of sputtered PMA films.

To explore the tunability of the small DMI in Pt/Co/Pt, samples with a thinner 1 nm Pt capping layer were fabricated, in order to increase the apparent SIA. Indeed, in Figure 2(c) it is observed that H_D has increased

significantly to the value 37 ± 1 mT. The change of efficiency ϵ_{SHE} matches with the change in layer thickness as discussed in the Supplementary Information. The SIA can be increased much more by replacing the top Pt layer by a different material, AIOx, as shown in Figure 2(e-f). In fact, H_D has become so large that we cannot quantify it within our setup. Regardless of the in-plane field, the domain-walls are chiral Néel walls which are pushed uniformly in the direction of current flow, hence opposite to conventional STT. A small linear effect of the in-plane field on the efficiencies appears to be present, which is either an experimental artifact or caused by mechanisms beyond our simplified 1D model. We verified this effect does not have the correct characteristics to be described by the Rashba effect, by quasi-statically reproducing the depinning process in the dynamic 1D DW model [3] including a current-dependent H_y Rashba field. Crucially, these results suggest that our Pt/Co/AIOx is not fundamentally different from Pt/Co/Pt, but only has a higher built-in chiral field due to the increased asymmetry.

Although the results presented so far here and by other authors [2, 3, 18, 19] match well with a SHE-induced torque dictated by the DW angle ϕ , it is not at all trivial that the DW indeed has the structure that these exper-

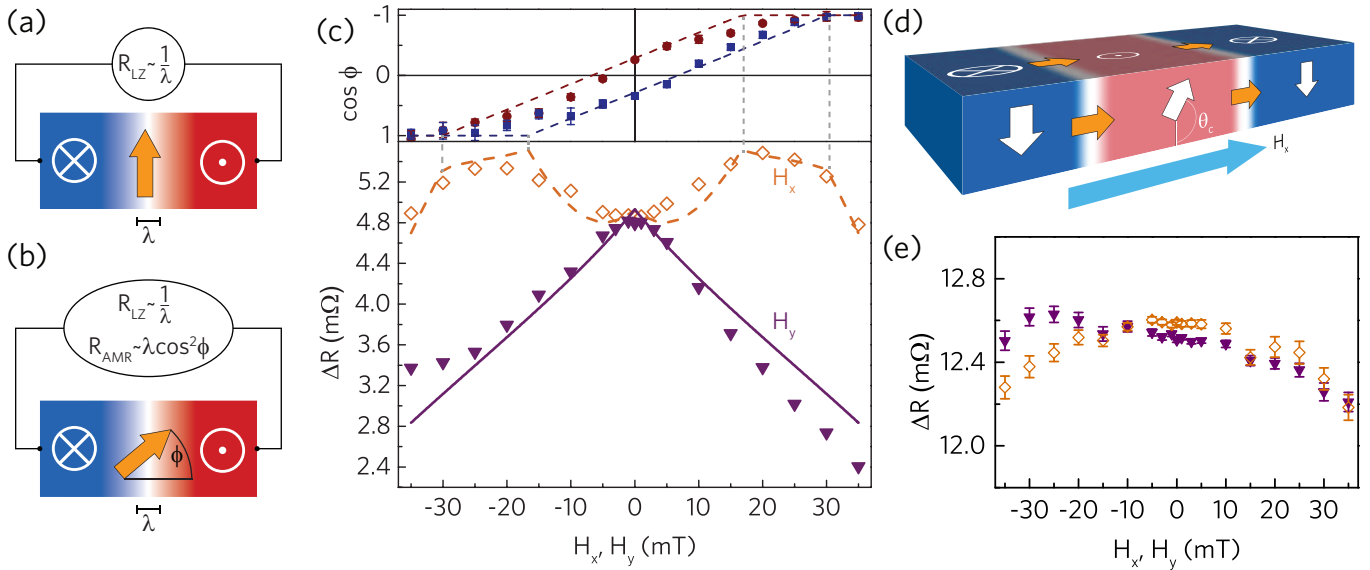


FIG. 3. Bloch-Néel transition revealed by DW resistance measurements. (a) a Bloch wall yields only an intrinsic contribution R_{LZ} to the DW resistance. (b) As ϕ approaches 0 (Néel wall), an additional contribution from the AMR effect arises. (c) (top) Depinning efficiency as a function of H_x and (bottom) Resistance change induced by 20 DWs of alternating polarity, as a function of H_x (open diamonds) and H_y (filled triangles), measured on the same Pt(4)/Co(0.5)/Pt(2) sample. The dashed orange and solid purple line are a fit including the two resistance contributions, in which H_K and H_D have been taken from the fit of the depinning data. The DW resistance peaks around $H_x = 20$ mT due to the transition from Bloch to Néel. A decreasing background signal is present in both the H_y and the H_x data due to canting of the magnetization in the irradiated domain (d), leading to a lower intrinsic contribution R_{LZ} . (e) DW resistance in Pt/Co/AlOx does not show the Bloch-Néel transition since Néel walls are highly stable.

iments suggest. In fact, the transition from a Bloch-like to a Néel state by an in-plane field was to our knowledge not measured before. We believe that using DW resistance as a probe for the DW structure is much more direct than using the DW mobility, since the resistance does not rely on any of the spin torques. Therefore, we have performed measurements of the DW resistance as a function of in-plane field. To be able to accurately measure tiny resistance changes induced by the DWs, we use lock-in measurements on an on-sample Wheatstone bridge[7, 26] consisting of four nominally identical wires, one of which has a Ga-irradiation pattern. To exclude magnetoresistive effects in the domains from polluting the measured resistance of the DWs, we measure the bias of the bridge for the monodomain state at each in-plane field, and subtract it from the bias in the presence of the multidomain state shown in Figure 1(e) (see also Methods section). When the resistance of a Bloch wall is measured (Figure 3(a)), the dominant contribution comes from the intrinsic resistance $R_{LZ} \sim 1/\lambda$ dictated by the Levy-Zhang model [6] for which we recently found experimental evidence [7, 26]. However, when the magnetization within the DW obtains a component parallel to the current flow (Figure 3(b)), an additional contribution R_{AMR} from anisotropic magnetoresistance arises [28], simply proportional to $\lambda \cos^2 \phi$.

Looking at the measured DW resistance in Pt(4)/Co(0.5)/Pt(2) as a function of H_x (open or-

ange diamonds in Figure 3(c)), we indeed see an increase when the in-plane field increases, owing to the transformation to a Néel wall. However, beyond $H_x = 30$ mT, the measured DW resistance starts to decrease again. This decrease is seen over the entire H_y -field range (purple triangles), which can be regarded as a kind of background measurement. We attribute this to a change of R_{LZ} related to the domain structure. Since the anisotropy in one of the domains is reduced strongly by the Ga irradiation treatment [8], this region tends to be pulled in plane, modifying the domain-wall profile as sketched in (Figure 3(d)). This has a strong effect on R_{LZ} , and also a small effect on R_{AMR} (see Supplementary Information for details of the model). From the DW-depinning data (top pane of Figure 3(c)), we can deduce $\phi(H_x, H_y)$, and use this as input in our resistance model. The best-fit to this model is presented as the dashed orange and solid purple lines in Figure 3(c)), where the free parameters are the anisotropy in the irradiated domain, the AMR resistivity, and the strength of the intrinsic DWR. The model reproduces the measurements, apart from two kinks at each field polarity (when the angles of either the 'red' or the 'blue' domain walls saturate, compare to top panel). It is not surprising that these sharp features from the 1D model become smooth in reality, especially since we measure the sum of 20 DWs, each with slightly different local properties.

Looking at the DW resistance measurements in Pt/Co/AlOx in Figure 3(e)), only minor changes as a function of in-plane field are observed, and there is no clear difference between the H_x and H_y data. Similar to the DW-depinning results, this suggests that the Néel character of the DWs is stabilized by a strong built-in chiral field and is not significantly influenced by the range of applied in-plane fields. The background due to magnetization canting is largely absent here, because the anisotropy in the irradiated domain is much higher. Although any change as a function of in-plane field is relatively small compared to the Pt(4)/Co(0.5)/Pt(2) sample, a small asymmetry appears in the H_y data, which may have the same unknown origin as the slight asymmetry in the DW depinning data in Figure 2(f).

We should note that, in our analysis so far, we assumed that the DW is oriented perpendicular to the nanowire, whereas it was recently demonstrated that the DW boundary might tilt in the xy -plane in systems with a significant DMI [18, 30]. Such tilting will occur when the DW moves at high speed (which is not applicable in depinning measurements), or when H_y fields are applied [30]. We estimate that the highest applied H_y of ~ 40 mT, could induce a tilting of at most 10° in Pt/Co/AlOx, which has the highest DMI. We do not observe significant tilting in the Kerr images (within the ~ 300 nm resolution), nor do we observe a dramatic difference between the DW resistance as a function of H_y and H_x in this material, hence the influence of this possible tilt angle is limited. Furthermore, in Pt/Co/Pt samples the DMI is an order of magnitude smaller, hence a tilting of at most 1 or 2 degrees might be induced, which is hardly significant and therefore not taken into account in the analysis.

We now briefly discuss the origin of the unexpected chiral effective fields in Pt/Co/Pt. It was recently calculated [31] that a significant DMI can arise in a Pt/Co bilayer, leading to a effective chiral field of several 100 mT. Since the chiral field in Pt/Co/Pt is the result of two canceling interfaces, we should stress that an imbalance between the DMI at the top and bottom interface of only a few percent is enough to achieve the measured magnitude. Ryu et al. [2] also studied the effect of stack asymmetry on the effective chiral field in Co/Ni multilayers, and concluded that the DMI originates at Pt/Co interfaces and scales with the thickness of the neighboring Co layer, which they attributed to proximity-induced moments in Pt. They concluded that DW motion in the direction of current flow implies that the DMI at the bottom interface dominates over the top interface. In the current manuscript, we appear to have tuned the DMI through the thickness of the Pt layers themselves. Due to growth-related phenomena, it is known that the top and bottom interface can have different characteristics, for example evidenced by a different contribution to the effective PMA [32]. Apparently, the DMI at the top interface decreases when reducing the top layer thickness, such that the net DMI increases. It is worth noting that

although the DMI at the top layer appears to decrease, the PMA constant increases for thinner Pt top layers (see Supplementary Information Table 1). In an inverted Pt(2)/Co/(0.5)/Pt(4) sample (Supplementary Information, Figure S1), it was found that the DMI almost vanishes, but does not change sign, thus the interfaces appear to become more symmetric for thick capping layers. This indeed suggests that interface characteristics are key, rather than the thickness of the layers themselves. Reasons for the top interface to vary with thickness can be changes to the mode of growth, different interdiffusion [32] or even slight oxidation at the top Co/Pt interface in case of thin capping layers.

To summarize, the effective chiral magnetic field in Pt/Co systems turns out to be tunable by varying the top layer thickness and material. The effect scales with the degree of structural inversion asymmetry and leads to a gradual change of the stable wall type from Bloch to Néel. Furthermore, by using the DW resistance as an independent measurement of the internal DW structure, a change of the internal structure from Bloch-like to Néel under longitudinal fields was evidenced, and correlated to the high efficiency of DW motion of Néel walls. These findings firmly establish SHE and DMI as a tandem for efficient and uniform domain wall motion.

I. METHODS

A. Sample fabrication

All samples consisted of $1.5\ \mu\text{m}$ wide strips fabricated on Si/SiO₂ substrates by Electron-Beam lithography, DC sputtering, and lift-off. The Pt(4)/Co(0.8)/Al(1.5) samples were oxidized in a 15 W, 0.1 mbar O₂ plasma for 10 minutes to obtain Pt/Co/AlOx. These samples were annealed for 20 minutes at 573 K. The Pt/Co/Pt samples did not undergo an annealing treatment. The samples were designed to form an on-sample Wheatstone bridge configuration to be able to measure resistance changes accurately (for details see [7]). The samples were locally irradiated with a 30 keV Ga FIB to make it possible to create a stable domain pattern with a well-defined number of domain walls. At the same time, the edges of the irradiation boundaries acted as pinning sites, to enable the well-controlled depinning measurements. The Ga doses were chosen to ensure that all DWs are stable during DWR measurements and amounted to 1.13×10^{13} ions/cm² on Pt/Co/AlOx, 0.50×10^{13} ions/cm² on Pt(4)/Co(0.5)/Pt(2) and Pt(4)/Co(0.4)/Pt(2), and 0.81×10^{13} ions/cm² on Pt(4)/Co(0.4)/Pt(1). Table S1 (Supplementary Information) provides the material parameters (PMA constant and M_s) obtained by VSM-SQUID magnetometry on unpatterned films.

B. DW depinning measurements

Very low DC current densities in the range $\pm 2 \times 10^{10}$ A/m² were used to exclude significant effects from Joule heating and Oersted fields. The current and in-plane field are kept constant, while the z -field is being ramped up until both DWs have depinned which is automatically detected by an image analysis routine. This is repeated at least 10 times for each current point to obtain sufficient signal to noise. Table S1 presents the fit parameters of the 1D model (H_K , H_D and ϵ_{SHE}) for each used material composition, and compares the latter to the expected efficiency ϵ_{calc} based on the layer thicknesses.

C. DW resistance measurements

Our measurement routine is very similar to what we described in [7]. We use a combination of an on-sample Wheatstone bridge and a lock-in technique to measure the resistance change due to the presence of domain walls. The in-plane field is applied constantly, and first the wire is saturated (zero DWs) by a negative H_z , and the lock-in voltage at $H_z \approx -1$ mT is recorded. Then, the domain walls are created by a positive H_z , the field is reduced to $H_z \approx 1$ mT and the lock-in voltage is recorded again. The difference is presented in Figure 3 as ΔR , and represents the resistance change due to all the DWs (20 or 18 for Pt/Co/Pt and Pt/Co/AlOx, respectively). Since the background voltage is recorded at the same in-plane

field as the voltage in the presence of DWs, magnetoresistive effects within the bulk of the domains, such as AMR due to canting or the magnon contribution [33], are automatically filtered out, leaving only resistance changes in the DW region. We always check the number and positions of the DWs present by real-time comparison to a Kerr-microscopy image. Furthermore, we always ensure that the magnetization underneath the 20 nm thick Pt contacts and the three reference strips in the bridge does not switch, as this can give rise to additional magnetoresistive signals. The small H_z during measurements serves to ensure the DW pattern remains stable during measurements. An AC probe current of 1 mA (0.75 mA) at 500 Hz was sent through two parallel series of Pt(4)/Co(0.5)/Pt(2) (Pt(4)/Co(0.8)/AlOx) wires and it was verified that a lower amplitude does not significantly alter the results. Because the bridge is not perfectly balanced, a bias of typically 10 mV occurs, even when all strips are magnetized in the same direction. When we introduce domain walls into one of the strips, the signal typically changes by 10 μ V. Note that a sample with slightly thicker $t_{\text{Co}} = 0.5$ nm had to be used, because the samples with $t_{\text{Co}} = 0.4$ turned out to be very easily switched by the spin Hall effect from the probe current. Therefore, much lower probe currents have to be used, and the thinner magnetic Co layer further deteriorates the signal/noise. Details on the modeling of in-plane field effects on the measured DW resistance are presented in the Supplementary Information, and the individual contributions to the modeled resistance are plotted in Figure S2.

-
- [1] Thiaville, A., Rohart, S., Jué, E., Cros, V. & Fert, A. Dynamics of Dzyaloshinskii domain walls in ultrathin magnetic films. *Europhys. Lett.* **100**, 57002 (2012).
 - [2] Emori, S., Bauer, U., Ahn, S.-M., Martinez, E. & Beach, G. S. D. Current-driven dynamics of chiral ferromagnetic domain walls. *Nat. Mater.* **12**, 611–6 (2013).
 - [3] Ryu, K.-S., Thomas, L., Yang, S.-H. & Parkin, S. Chiral spin torque at magnetic domain walls. *Nat. Nanotechnol.* **8**, 527–33 (2013).
 - [4] Je, S.-G. *et al.* Asymmetric magnetic domain-wall motion by the Dzyaloshinskii-Moriya interaction. *Phys. Rev. B* **88**, 214401 (2013).
 - [5] Parkin, S. S. P., Hayashi, M. & Thomas, L. Magnetic domain-wall racetrack memory. *Science* **320**, 190–4 (2008).
 - [6] Thiaville, A., Nakatani, Y., Miltat, J. & Suzuki, Y. Micromagnetic understanding of current-driven domain wall motion in patterned nanowires. *Europhys. Lett.* **69**, 990 (2005).
 - [7] Miron, I. M. *et al.* Perpendicular switching of a single ferromagnetic layer induced by in-plane current injection. *Nature* **476**, 189–194 (2011).
 - [8] Liu, L. *et al.* Spin-Torque Switching with the Giant Spin Hall Effect of Tantalum. *Science* **336**, 555–558 (2012).
 - [9] Garello, K. *et al.* Symmetry and magnitude of spin-orbit torques in ferromagnetic heterostructures. *Nat. Nanotechnol.* **8**, 587–93 (2013).
 - [10] Miron, I. M. *et al.* Fast current-induced domain-wall motion controlled by the Rashba effect. *Nat. Mater.* **10**, 419–23 (2011).
 - [11] Wang, X. & Manchon, A. Diffusive Spin Dynamics in Ferromagnetic Thin Films with a Rashba Interaction. *Phys. Rev. Lett.* **108**, 117201 (2012).
 - [12] Kim, K.-W., Seo, S.-M., Ryu, J., Lee, K.-J. & Lee, H.-W. Magnetization dynamics induced by in-plane currents in ultrathin magnetic nanostructures with Rashba spin-orbit coupling. *Phys. Rev. B* **85**, 180404(R) (2012).
 - [13] Hirsch, J. Spin Hall Effect. *Phys. Rev. Lett.* **83**, 1834–1837 (1999).
 - [14] Haazen, P. P. J. *et al.* Domain wall depinning governed by the spin Hall effect. *Nat. Mater.* **12**, 299 (2013).
 - [15] Khvalkovskiy, A. V. *et al.* Matching domain-wall configuration and spin-orbit torques for efficient domain-wall motion. *Phys. Rev. B* **87**, 020402 (2013).
 - [16] Moore, T. A. *et al.* High domain wall velocities induced by current in ultrathin Pt/Co/AlOx wires with perpendicular magnetic anisotropy. *Appl. Phys. Lett.* **93**, 262504 (2008).

- [17] Koyama, T. *et al.* Current-Induced Magnetic Domain Wall Motion in a Co/Ni Nanowire with Structural Inversion Asymmetry. *Appl. Phys. Express* **6**, 033001 (2013).
- [18] Emori, S., Martinez, E. & Bauer, U. Spin Hall torque magnetometry of Dzyaloshinskii domain walls. *arXiv* **1308.1432** (2013).
- [19] Torrejon, J. *et al.* Interface control of the magnetic chirality in TaN—CoFeB—MgO heterostructures. *arXiv* **1308.1751** (2013).
- [20] Moriya, T. New mechanism of anisotropic superexchange interaction. *Phys. Rev. Lett.* **4**, 228 (1960).
- [21] Heide, M., Bihlmayer, G. & Blügel, S. Dzyaloshinskii-Moriya interaction accounting for the orientation of magnetic domains in ultrathin films: Fe/W(110). *Phys. Rev. B* **78**, 140403 (2008).
- [22] Chen, G. *et al.* Novel Chiral Magnetic Domain Wall Structure in Fe/Ni/Cu(001) Films. *Phys. Rev. Lett.* **110**, 177204 (2013).
- [23] Chen, G. *et al.* Tailoring the chirality of magnetic domain walls by interface engineering. *Nat. Commun.* **4**, 2671 (2013).
- [24] Franken, J. H. *et al.* Precise control of domain wall injection and pinning using helium and gallium focused ion beams. *J. Appl. Phys.* **109**, 07D504 (2011).
- [25] Franken, J. H., Hoeijmakers, M., Swagten, H. J. M. & Koopmans, B. Tunable Resistivity of Individual Magnetic Domain Walls. *Phys. Rev. Lett.* **108**, 037205 (2012).
- [26] Aziz, A. *et al.* Angular Dependence of Domain Wall Resistivity in Artificial Magnetic Domain Structures. *Phys. Rev. Lett.* **97**, 206602 (2006).
- [27] Levy, P. M. & Zhang, S. Resistivity due to Domain Wall Scattering. *Phys. Rev. Lett.* **79**, 5110–5113 (1997).
- [28] Koyama, T. *et al.* Observation of the intrinsic pinning of a magnetic domain wall in a ferromagnetic nanowire. *Nat. Mater.* **10**, 194–197 (2011).
- [29] Franken, J. H., Hoeijmakers, M., Lavrijsen, R. & Swagten, H. J. M. Domain-wall pinning by local control of anisotropy in Pt/Co/Pt strips. *J. Phys. Cond. Matter* **24**, 024216 (2012).
- [30] Boulle, O. *et al.* Domain Wall Tilting in the Presence of the Dzyaloshinskii-Moriya Interaction in Out-of-Plane Magnetized Magnetic Nanotracks. *Phys. Rev. Lett.* **111**, 217203 (2013).
- [31] Freimuth, F., Blügel, S. & Mokrousov, Y. Berry phase theory of Dzyaloshinskii-Moriya interaction and spin-orbit torques. *arXiv* **1308.5983** (2013).
- [32] Bandiera, S., Sousa, R. R., Rodmacq, B. B. & Dieny, B. Asymmetric Interfacial Perpendicular Magnetic Anisotropy in Pt/Co/Pt Trilayers. *IEEE Magn. Lett.* **2**, 3000504 (2011).
- [33] Nguyen, V. D. *et al.* Detection of Domain-Wall Position and Magnetization Reversal in Nanostructures Using the Magnon Contribution to the Resistivity. *Phys. Rev. Lett.* **107**, 136605 (2011).

ACKNOWLEDGEMENTS

This work is part of the research programme of the Foundation for Fundamental Research on Matter (FOM), which is part of the Netherlands Organisation for Scientific Research (NWO).

AUTHOR CONTRIBUTIONS

J.H.F. designed the experiments and prepared the manuscript. M.H. and J.H.F. performed the experiments and the data analysis. H.J.M.S. and B.K. assisted in the analysis and commented on the final manuscript.

Supplementary Information: Tunable chiral spin texture in magnetic domain-walls

S1. MATERIAL PARAMETERS

	M_s MA/m	K_{eff} MJ/m ³	$\mu_0 H_D$ mT	$\mu_0 H_K$ mT	ϵ_{SHE} 10 ⁻¹⁴	ϵ_{calc} TA ⁻¹ m ²	ν
Pt(4)/Co(0.36)/Pt(1)	1.01(5)	0.39(2)	37(1)	37(1)	6.4(2)	6.7	0.68
Pt(4)/Co(0.36)/Pt(2)	1.08(5)	0.27(1)	12.5(4)	24.6(5)	2.76(6)	3.2	0.34
Pt(4)/Co(0.8)/AlOx(1.9)	1.17(5)	0.28(1)	≥ 40	?	4.43(6)	3.4	0.89
Pt(4)/Co(0.5)/Pt(2)	1.07(5)	0.28(1)	11(2)	37(1)	2.4(1)	2.3	0.34
Pt(2)/Co(0.5)/Pt(4)	1.18(5)	0.22(1)	3(1)	19(2)	-1.8(1)	-2.1	-0.34

Table S1. Fit parameters and material properties of various compositions.

Table S1 summarizes the measured material properties. M_s and K_{eff} have been measured by VSM-SQUID magnetometry of unpatterned films. The samples labeled with a Co thickness of 0.4 nm in the text for convenience, were actually 0.36 nm thick. $\mu_0 H_D$, $\mu_0 H_K$, and ϵ_{SHE} have been obtained by fits of the DW depinning data like in Figure 2 in the main text. Although a stronger spin Hall current is injected in Pt/Co/AlOx, ϵ_{SHE} is smaller than in Pt/Co/Pt(1 nm) because it is absorbed by a thicker Co layer (see equation (1) in the main text). The inverted stack Pt(2)/Co(0.5)/Pt(4) also has an inverted ϵ_{SHE} , as we already explained in [S1]. Figure S1 provides a new measurement of the depinning efficiency as a function of H_x on this layer system, in order to reveal the presence of DMI. There is a very small opening visible, indicative of a H_D with the same sign as the inverted composition. Actually, it seems like one of the DWs has zero H_D (crosses through the origin), whereas the other one has a small but finite H_D . In any case, this suggests that the DMI, unlike the SHE, is not a result of the Pt layer thicknesses themselves, but rather the effect of increasing asymmetry between the top and bottom interface when the top layer is varied.

Since both DMI and PMA are expectedly interface effects, it is interesting to look for correlations between the parameters H_D and K_{eff} . For the Pt/Co/Pt samples, there is indeed a positive correlation between H_D and K_{eff} . However, Pt/Co/AlOx breaks this trend: it has a much stronger H_D than any other sample whereas K_{eff} is similar, so the two parameters are definitely not always directly related. Given that the DW motion is in the direction of current flow, we know that the DMI at the bottom interface must be dominant over the DMI from the top interface [S2]. So in fact, the DMI at the top interface must *decrease* when the top layer is made thinner, whereas the anisotropy contribution from this interface is actually seen to *increase*. So there appears to be a *negative* correlation between the anisotropy and DMI at the top interface, leading to a *positive* correlation between the anisotropy and the total DMI which is dominated by the bottom Pt/Co interface.

S1.1. Spin Hall amplitudes

In the last two columns of Table S1, we have calculated the expected loss factor ν of the spin Hall effect, and the accompanying depinning efficiency of Néel walls in the 1D model [S3],

$$\epsilon_{\text{calc}} = \frac{\pi \hbar \nu \theta_{\text{SH}}}{4eM_s t}. \quad (\text{S1})$$

The calculation of ν is straightforward; the net spin Hall current due to a *single* thin Pt layer with thickness t_{Pt} is given by [S4]

$$J_S(t_{\text{Pt}}) = \theta_{\text{SH}} J \left(1 - \text{sech} \left(\frac{t_{\text{Pt}}}{\lambda_{\text{sf}}} \right) \right), \quad (\text{S2})$$

where $\lambda_{\text{sf}} \approx 1.4$ nm the spin diffusion length of Pt [S5] and $\theta_{\text{SH}} = 0.07$ the spin Hall angle of Pt [S5]. For a Co layer sandwiched between two Pt layers, two of these spin currents with opposite polarization are injected, yielding a net spin current

$$J_S^{\text{eff}} = \nu \theta_{\text{SH}} J := \left(\text{sech} \left(\frac{t_{\text{Pt}}^{\text{top}}}{\lambda_{\text{sf}}} \right) - \text{sech} \left(\frac{t_{\text{Pt}}^{\text{bottom}}}{\lambda_{\text{sf}}} \right) \right) \theta_{\text{SH}} J. \quad (\text{S3})$$

Comparing the calculated ϵ_{calc} to the measured ϵ_{SHE} in Table S1, we observe close agreement. The largest deviation is found in Pt/Co/AlOx which measures a slightly higher ϵ_{SHE} than expected. We should note that this is the only sample that has undergone an annealing treatment, hence it might have different properties compared to the other ones. There might also be a contribution from conventional STT to ϵ_{SHE} in Pt/Co/AlOx, but since conventional STT would oppose the SHE torque, this should reduce the measured ϵ_{SHE} compared to the model, whereas the difference we observe is opposite.

S2. DW RESISTANCE MODEL

In this section, we propose a model to describe the two dominant contributions to the DW resistance. We first apply the Levy-Zhang model of the intrinsic resistivity to the expected DW profile in the sample. Then, we discuss the contribution from anisotropic magnetoresistance (AMR). Finally, an expression is given for the measured resistance change in an actual Pt/Co/Pt layer, where current shunts through the Pt layers. This expression is fitted to the experimental data.

S2.1. Levy-Zhang model for arbitrary DW profiles

The Levy-Zhang model describes the contribution to DW resistance due to spin mistracking [S6]. In their original derivation, they assume a simplified DW profile of the form $\theta(x) = \pi x/d$. However, in reality the DW has the more complicated Bloch profile, and when magnetization canting due to an in-plane field starts to play a role, the actual profile is even more complex. We therefore first derive an expression valid for any DW profile, and then insert an approximated ‘canted’ profile to find an expression for R_{LZ} as a function of in-plane field.

The original result of DW resistivity by Levy and Zhang for a current perpendicular to the DW reads

$$\rho_{\text{LZ}} = C \left(\frac{\pi}{\lambda} \right)^2, \quad (\text{S4})$$

with λ the DW width and C a prefactor given by

$$C = \frac{\hbar^4 k^2 \rho_0}{80 J^2 m^2} \left(\frac{\rho_{\uparrow}}{\rho_{\downarrow}} - 2 + \frac{\rho_{\downarrow}}{\rho_{\uparrow}} \right) \left(3 + \frac{10 \sqrt{\rho_{\uparrow}/\rho_{\downarrow}}}{\rho_{\uparrow}/\rho_{\downarrow} + 1} \right), \quad (\text{S5})$$

with \hbar Planck’s constant, $k \approx 1 \text{ \AA}^{-1}$ the Fermi wavevector, m the electron mass, $J \approx 0.5 \text{ eV}$ the (microscopic) exchange splitting, $\rho_{\uparrow}/\rho_{\downarrow}$ the spin asymmetry in the Co layer, and ρ_0 the resistivity of the Co layer.

(S4) was obtained for the simple DW profile with a constant slope $d\theta/dx = \pi/\lambda$. For a real DW in which this slope is not constant, the resistivity is position-dependent within the DW. Therefore, a more general form of the DW resistivity is

$$\rho_{\text{LZ}} = C \left(\frac{d\theta(x)}{dx} \right)^2. \quad (\text{S6})$$

The DW resistance is found by integrating the resistivity over the entire DW profile,

$$R_{\text{LZ}}(x) = \frac{1}{S} \int_{-\infty}^{\infty} C \left(\frac{d\theta(x)}{dx} \right)^2 dx, \quad (\text{S7})$$

with S the cross-sectional area of the magnetic layer.

As explained briefly in the main text, we expect at high in-plane fields a DW profile that rotates from $\theta = 0$ in the non-irradiated region, to $\theta_c(H_x) < \pi$ in the Ga-irradiated region, where the anisotropy has decreased so much that the magnetization is significantly pulled in-plane. We assume a scaled Bloch profile that takes into account this smaller final angle of the DW,

$$\theta(x) = \frac{2}{\pi} \theta_c(H_x) \arctan \left(e^{x/\lambda} \right), \quad (\text{S8})$$

where we use $\lambda = \sqrt{A/K_{\text{low}}}$ with $A = 16 \text{ pJ/m}$ and K_{low} the effective anisotropy in the irradiated region (a fit parameter), which is seen to determine the DW width in micromagnetic simulations. From the Stoner-Wohlfarth

model, it is straightforward to derive that the magnetization canting as a function of in-plane field is given by

$$\theta_c(H_x) = \pi - \arcsin\left(\frac{H_x M_s}{2K_{\text{low}}}\right). \quad (\text{S9})$$

Plugging the DW profile of (S8) into the expression for the resistance (S8) yields

$$R_{\text{LZ}}(H_x) = \frac{2C}{S} \frac{\left(\pi - \arcsin\left(\frac{H_x M_s}{2K_{\text{low}}}\right)\right)^2}{\pi^2 \lambda}. \quad (\text{S10})$$

Note that we used H_x in the expressions above, but the same expressions hold for H_y .

S2.2. AMR contribution

The AMR resistivity within the DW scales with the square of the projection of the magnetization on the x -axis, hence

$$\rho_{\text{DWAMR}}(x) = \rho_{\text{AMR}} \cos^2 \phi \sin^2 \theta(x), \quad (\text{S11})$$

where ρ_{AMR} is the AMR resistivity parameter of Co. We will assume that the angle ϕ does not vary within the DW (which is supported by micromagnetic simulations). $\phi = 0$ represents a Néel wall, giving the highest AMR.

If there is no DW present and no canting of the magnetization, the additional AMR contribution in the presence of DWs is found by integrating (S11). However, if one of the domains is canted in the x -direction, there is a large contribution from this domain to the AMR. This is however not the experimental situation, because the subtracted background signal is recorded at the same in-plane field, hence AMR from the domains is not included in the presented DW resistance. Since we do not have an analytical expression for this background, we start from the original Bloch profile which rotates from 0 to π so that the integral to infinity converges, and multiply (S11) by a correction factor $\cos^2 \theta_c(H_x)$ which is not analytical but at least correct in the center of the domain wall,

$$\rho_{\text{DWAMR}}(x) = \rho_{\text{AMR}} \cos^2 \phi \sin^2 \theta(x) \cos^2 \theta_c(H_x). \quad (\text{S12})$$

Now we only need to integrate the resistivity to get the AMR contribution to the DW resistance,

$$R_{\text{AMR}} = \frac{1}{S} \int_{-\infty}^{\infty} \rho_{\text{DWAMR}} dx = \frac{1}{S} \frac{\rho_{\text{AMR}} \lambda (4K_{\text{low}}^2 - H_x^2 M_s^2) \cos^2 \phi}{2K_{\text{low}}^2}. \quad (\text{S13})$$

S2.3. Converting to actually measured resistance change

The actually measured resistance change is reduced strongly by current shunting through the Pt layers. Assuming only a fraction $p \approx 0.03$ of the current runs through the Co layer in Pt/Co/Pt based on a Fuch-Sondheimer model [S7], the resistance of the wire R_{wire} can be described as the result of two parallel resistors $R_{\text{Co}} = \frac{R_{\text{wire}}}{p}$ and $R_{\text{Pt}} = \frac{R_{\text{wire}}}{1-p}$. The occurrence of N DWs only trigger a resistance change of the Co layer ΔR_{Co} ,

$$\Delta R_{\text{Co}} = N(R_{\text{LZ}} + R_{\text{AMR}}). \quad (\text{S14})$$

In the parallel resistor model, it is easy to show that this leads to a resistance change of the whole wire of

$$\Delta R = \frac{Np^2(R_{\text{LZ}} + R_{\text{AMR}})R_{\text{wire}}}{R_{\text{wire}} - N(p-1)p(R_{\text{LZ}} + R_{\text{AMR}})}. \quad (\text{S15})$$

In the Pt(4)/Co(0.5)/Pt(2) wire, $R_{\text{wire}} = 1.3 \text{ k}\Omega$ and $N = 20$, whereas in the Pt/Co/AlOx wire, $R_{\text{wire}} = 1.8 \text{ k}\Omega$ and $N = 18$

This model for ΔR has been fitted to the DWR data in Figure 3(c) in the main text, with ρ_{AMR} , C , and K_{low} as free parameters. The value for ρ_0 in the prefactor C was calculated as $R_{\text{Co}} S/L$, with L the length of the wire. Note that a dependence on the DW angle ϕ enters in the model via R_{AMR} . The value of ϕ at each H_x and H_y are described by minimization of Eqn. (1) in the main text, where H_D and H_K are extracted from the DW depinning data (see table S1). The best fit was obtained with parameters $\rho_{\text{AMR}} = 2.9 \times 10^{-9} \Omega\text{m}$, $C = 2.25 \times 10^{-24} \Omega\text{m}^3$, $K_{\text{low}} = 29.8 \text{ kJ/m}^3$.

The value of the prefactor C implies via (S5) that $\rho_{\uparrow}/\rho_{\downarrow} \approx 15$, which is reasonable according to the original paper by Levy and Zhang [S6]. The value for K_{low} at a dose of 0.50×10^{13} ions/cm² is somewhat lower than we measured before [S8], which could relate to some of the assumptions in our modeling, such as the chosen values of the fixed parameters or the assumption that the DW width does not depend on in-plane field. Note that we did not have to include additional magnetoresistance effects such as the geometric size effect or the anisotropic interface magnetoresistance [S9] to obtain a reasonable fit. The presence of such an effect could alter the fit parameters, but our main conclusion that Bloch walls transform to Néel walls is robust simply because of the very different response to x and y fields, regardless of the precise relative magnitude of the effects that are responsible for the measured changes.

In Figure S2, we have plotted the various contributions that make up the fitted curves in Figure 3(c) (main text). The purple solid line indicates the intrinsic DW resistance as a function of in-plane field, which gives the same result for H_x and H_y fields. The dark blue dotted line shows the modeled contribution from the AMR effect under the influence of H_x fields. The light blue dash-dotted line shows a calculation of what the AMR effect would look like if we would not take into account the magnetization canting: the AMR resistance simply saturates at high H_x . The contribution from AMR as a function of H_y (dashed green curve) is quite small, and reduces at higher in-plane fields since the DW loses its slight Néel character. Note that, since we always measure DWs of both polarities in experiment, the modeled AMR under H_x fields is a superposition of two curves, mutually shifted by the chiral field $\frac{2}{\pi}H_D$.

SUPPLEMENTARY REFERENCES

-
- [S1] Haazen, P. P. J. *et al.* Domain wall depinning governed by the spin Hall effect. *Nat. Mater.* **12**, 299 (2013).
[S2] Ryu, K.-S., Thomas, L., Yang, S.-H. & Parkin, S. Chiral spin torque at magnetic domain walls. *Nat. Nanotechnol.* **8**, 527–33 (2013).
[S3] Thiaville, A., Rohart, S., Jué, E., Cros, V. & Fert, A. Dynamics of Dzyaloshinskii domain walls in ultrathin magnetic films. *Europhys. Lett.* **100**, 57002 (2012).
[S4] Liu, L., Moriyama, T., Ralph, D. C. & Buhrman, R. A. Spin-Torque Ferromagnetic Resonance Induced by the Spin Hall Effect. *Phys. Rev. Lett.* **106**, 036601 (2011).
[S5] Liu, L., Buhrman, R. A. & Ralph, D. C. Review and Analysis of Measurements of the Spin Hall Effect in Platinum. *arXiv* **1111.3702** (2011).
[S6] Levy, P. M. & Zhang, S. Resistivity due to Domain Wall Scattering. *Phys. Rev. Lett.* **79**, 5110–5113 (1997).
[S7] Franken, J. H., Hoeijmakers, M., Swagten, H. J. M. & Koopmans, B. Tunable Resistivity of Individual Magnetic Domain Walls. *Phys. Rev. Lett.* **108**, 037205 (2012).
[S8] Franken, J. H., Hoeijmakers, M., Lavrijsen, R. & Swagten, H. J. M. Domain-wall pinning by local control of anisotropy in Pt/Co/Pt strips. *J. Phys. Cond. Matter* **24**, 024216 (2012).
[S9] Kobs, A. *et al.* Anisotropic Interface Magnetoresistance in Pt/Co/Pt Sandwiches. *Phys. Rev. Lett.* **106**, 217207 (2011).

SUPPLEMENTARY FIGURES

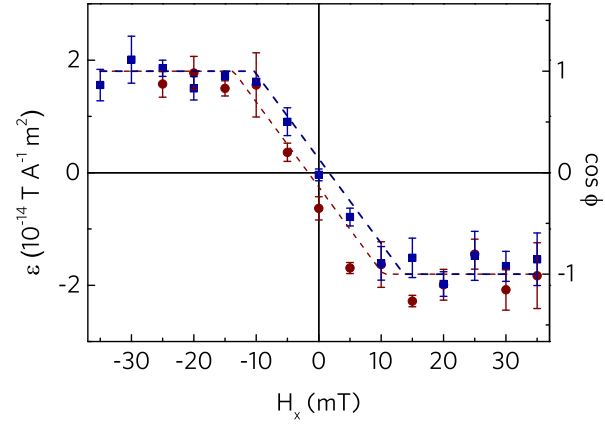


Figure S1. Depinning efficiency as a function of H_x on the inverted stack Pt(2)/Co(0.5)/Pt(4).

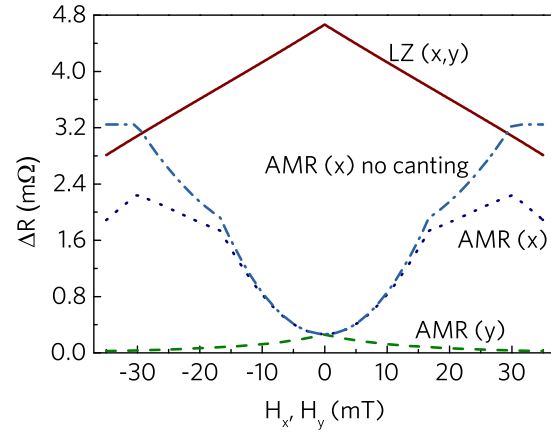


Figure S2. Contributions of the various domain wall resistance effects as a function of in-plane field. Plotted are the intrinsic Levy-Zhang contribution (solid red line), the DW AMR as a function of H_y (dashed green line) and H_x (dotted dark-blue line), and the (hypothetical) DW AMR contribution as a function of H_x in the absence of magnetization canting (dash-dotted light-blue line). The kinks occur when one of the two present domain-wall types reach the Néel state, and there are two of them on both sides because they are shifted in opposite directions by the effective chiral fields.